

Heterogeneity and Distortion in Shelled Binder Jet Geometries in Green and Sintered Parts

Madi Lawrence, Nathan B. Crane

Department of Mechanical Engineering, Brigham Young University, Provo, UT 84602

Abstract

Binder Jetting (BJ) has many advantages as an additive manufacturing process, but one of its major disadvantages is that it can be difficult to achieve high density final parts. Pores in BJ parts negatively impact the mechanical strength and ductility and limit the usefulness of BJ parts in demanding industries. Multiple studies show that shell printing can be used to increase part density, but the mechanisms that contribute to low density in bound regions are poorly understood. This study uses X-ray computed tomography (XCT) scanning to explore the internal structures of shelled parts and provides insight into the mechanisms of density defects in printed regions. The work shows that layers have a strong impact on porosity in printed regions but not in unbound regions and that density is reduced near the boundaries between bound and unbound regions. The differences between bound and unbound regions causes curvature in asymmetric parts during sintering.

Introduction

Binder Jetting (BJ) is an additive manufacturing process where particles are bound together using tiny droplets of liquid binder. This “green” part is later post-processed to achieve final properties—typically by sintering. Advantages of BJ printing over other additive manufacturing methods include low costs, fast build rates, and a wide variety of possible printable materials. However, unintended voids in printed parts known as porosity defects are commonly found in BJ printed parts. Porosity defects reduce the density, strength, and ductility of BJ parts which limit the technology’s applications in demanding industries [1, 2].

Figure 1 shows the main steps of the BJ print process: powder spreading, rolling, and inkjet printing [3]. After the print process, there are several additional post processing steps (Figure 2). First, the binder is cured and bound together parts are removed from the loose powder in the bed. At this stage, the parts are considered “green,” meaning the powder particles are glued together in the desired shape, but the parts are weak and not at the final desired density. Parts printed in metal powders are typically only about 50-60% of the bulk material density [4]. The final step is sintering, where BJ parts are placed in a high temperature furnace to fuse the individual powder particles together to reach final part density and other material properties [5].

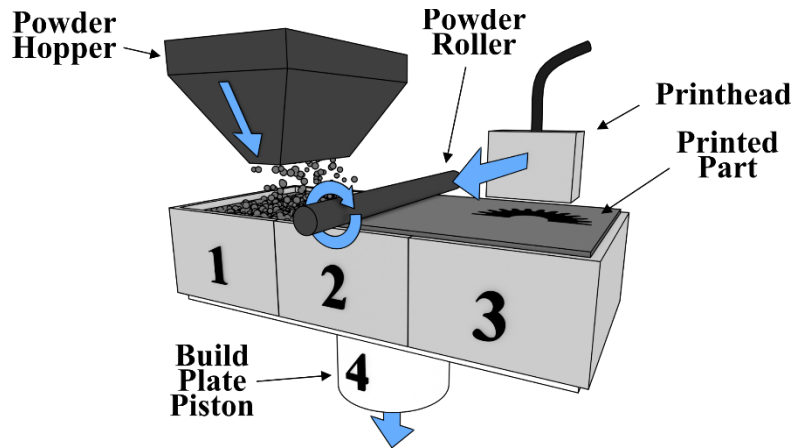


Figure 1. BJ Print Process 1) Powder is deposited. 2) The roller smooths and compacts the powder. 3) Inkjet printhead deposits liquid binder. 4) The build bed is lowered, and the process is repeated.

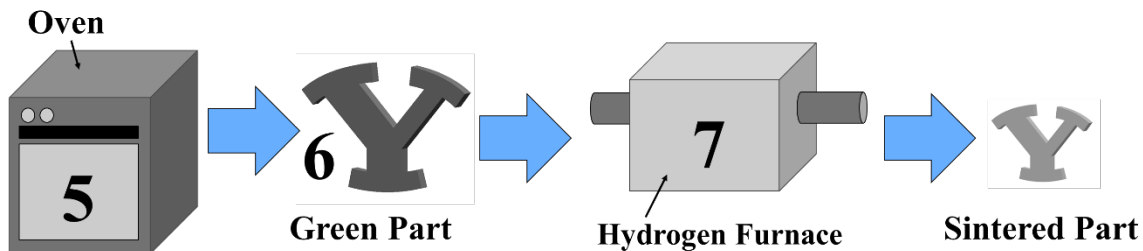


Figure 2. BJ Post Processing Steps 5) Curing and depowdering. 6) Green part. 7) Sintering. 8) Final Sintered Part.

Several recent studies propose “shelled printing” as a method to reduce porosity defects in BJ [6-8]. In the shelled printing method, parts are created with regions of enclosed unbound powder surrounded by regions of bound powder. These shell printing studies use various materials, but each show that bound areas exhibit more porosity defects and lower part densities than nearby unbound regions. [7]. For example, Li et al. [6] showed density reduced by 5-10% in bound regions when printing a free flowing alumina powder. Salim et al. [8] showed that unbound regions of shelled parts printed in 420SS and infiltrated with copper had on average 16% less bronze than the bound regions. Shell printing studies propose various explanations for the phenomenon observed, including residual carbon from deposited binder [7, 9, 10], poor powder compaction in printed areas [6, 8], and powder rearrangement due to binder droplet impact [3, 11, 12].

In this study, samples were printed with arrangements of bound and unbound powder to study the impact of shelled parts on the part density. These impacts were measured by measuring the mass and density, and micro-XCT analysis of the green and sintered parts. Samples were also designed to assess the impact of asymmetric trapped powder regions on the final sintered geometry.

Methods

Print Parameters

All parts in this study were printed on a ExOne Innovent+ BJ printer, using Sandvik Osprey SS316L powder with mean particle diameter (dv50) of 10 μm (dv10 of 3.92 μm and a dv90 of 22.0 μm), and ExOne aqueous binder. Standard print parameters were used for this machine and material combination based on previous experimentation. See Table 1 for details. Parts were cured at 180°C for 4-6 hours before depowdering. Figure 3 shows the coordinate system used throughout this study relative to the printing and rolling axes of the ExOne Printer. The X axis is in the direction the roller moves the powder, the Y axis along the axis of printhead motion, and the Z axis is in the build direction of the layers.

Table 1. Summary of print parameters

<i>Parameter</i>	<i>Value</i>
Layer Thickness	40 μm
Target Saturation	70 %
Recoat Speed	~500 mm/sec
Roller Traverse Speed	3 mm/sec
Roller Rotation Speed	600 rpm
Drying Time	24 sec
Target Bed Temp	40°C

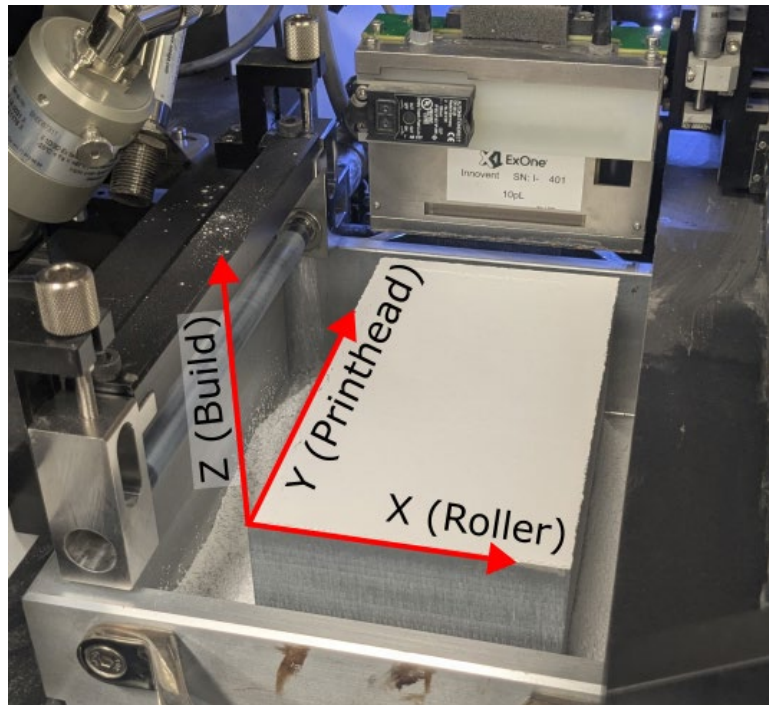


Figure 3. Coordinate axes used throughout this study relative to the ExOne Innovate+ printhead and roller motion.

Part Geometries and Experimental Design

Shells thinner than 1 mm were found to be fragile and hard to work with in the green state, so this study primarily used parts with a 1mm shell thickness, such as those shown in Figure 4a. These 1mm shelled XCT cubes were used for both the green and sintered XCT scans and have an internal horizontal wall of bound powder to show transitions at the top and bottom surfaces of bound powder in a single scan. Larger asymmetrical shelled parts (Figure 4b) were used to show the potential effects of uneven sections in shelled parts on sintered part shape. These parts were labeled to indicate whether the unbound region was towards the front or back (along the y axis) of the part during printing. Parts were sintered in the same orientation and order they were printed, but perpendicular to the axis of the furnace tube, to mitigate any confounding effects of uneven heating during sintering.

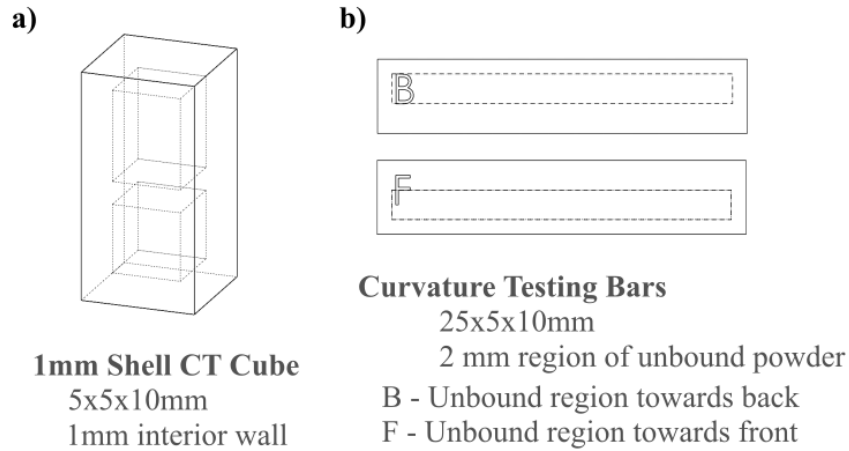


Figure 4. CAD drawings of the samples used in this study. Dashed lines represent hollow areas of the CAD model, which will result in unbound regions in the BJ parts. a) 1 mm Shell XCT Cube – used for green and sintered scans, has interior horizontal wall. b) Curvature Testing Bars – off-center unbound region

To further assess the effect of print orientations and unbound region size on shelled part behavior, identical shelled parts with thin slots (1.5 mm and 0.75 mm wide) of unbound powder were printed. These were printed with varied orientations so that the long dimension of the slot oriented either in the printhead (Y) or roller (X) direction (Figure 5). This permits observation of the impact of powder spreading near the boundaries between bound and unbound regions on the green part structure.

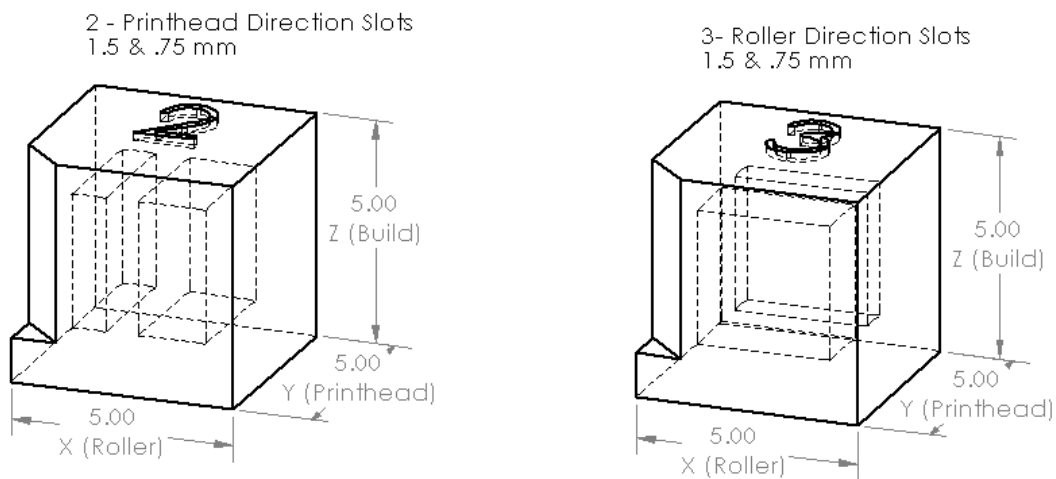


Figure 5. Drawing of orientation slot parts. Notched corners and labels were used to maintain part orientation at each step of the process.

Each part type was distributed around the bed to control for location-based density variation, especially between the side where powder rolling commences (leading edge) and ends (trailing edge) of the bed. See Figure 6 for a sample layout. Comparisons in this study were made between parts printed in the same bed to reduce the effects of run-to-run variation due to environmental or other factors.

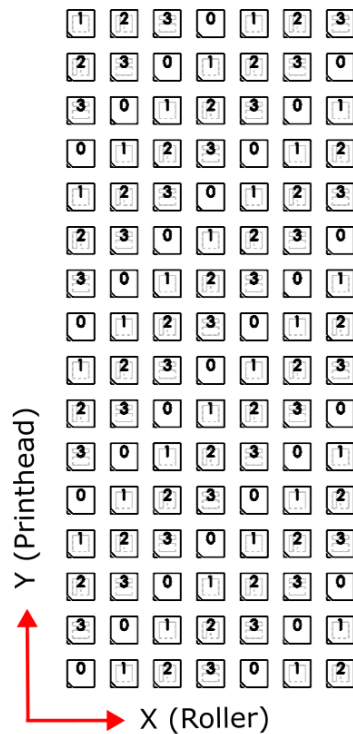


Figure 6. Example of cube layout used, with varying print bed locations by part type. Each number represents a different type of part, as shown in Figure 5, similar distribution of parts by type was used for other beds and cube types. Roller and printhead directions for the printer are also indicated.

Sintering

Some of the shelled parts were sintered to further analyze the effects of shelled geometries. All parts were sintered in a hydrogen atmosphere with a CM 1600 Series Model 2630-20 HT furnace, with a 4 inch diameter tube and a flow rate of approximately 4.7 liters/min (10 SCFH), shown in Figure 7. The sintering profile used is outlined in Figure 8. The temperature was held for 1 hour at 600°C to burn out any remaining binder, before the parts were sintered to 1350°C [13, 14].



Figure 7. CM Hydrogen Furnace used in this study.

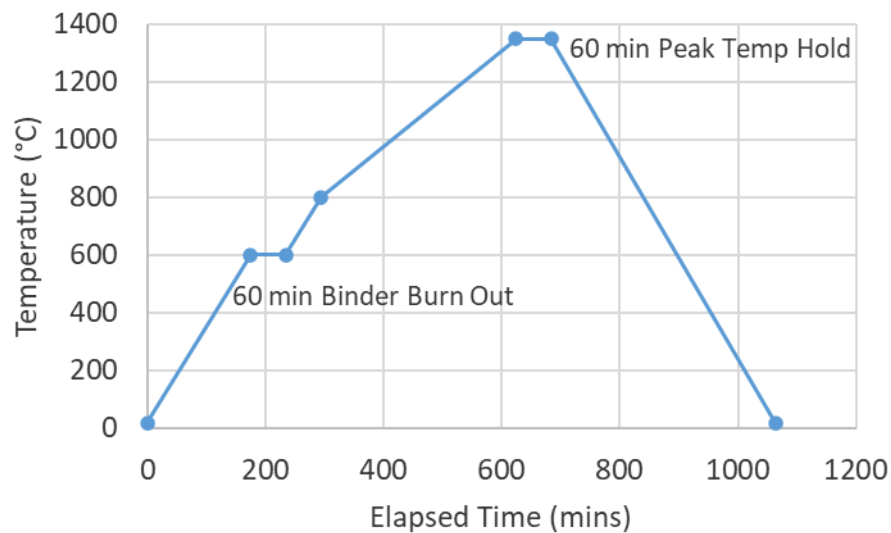


Figure 8. Sintering Profile used in this study. Sintering was done in a hydrogen atmosphere to a peak temperature of 1350°C, with a binder burn out phase at 600°C. Ramp rates were chosen based on furnace limitations.

Total Part Density

Overall density of green BJ parts was estimated by taking the ratio of mass to CAD model volume. The Archimedes method was used to measure sintered part density.

XCT Scanning and Analysis

Micro XCT scans were performed using a Zeiss Xradia Versa 620 3D X-ray Microscope/Nano-XCT. Settings were chosen according to the manufacturer's guidelines for transmittance and exposure, to achieve voxel sizes between 4-6 μm with beam hardening compensation. This allowed for pores and layers to be visible, as well as trends in density to be observed. Time and cost constraints limited the number of samples that could be feasibly XCT scanned, so the samples chosen are intended to be representative of other similar parts.

Analysis was conducted using ImageJ and Python to manipulate and analyze the stacks of TIFF images generated from XCT scans. ImageJ was primarily used to straighten the raw XCT images to better align the image stacks with the print sample axis, as well as crop the image for analysis of certain sections (i.e., only the unbound region of a sample). Python was used to average and plot pixel intensity along different axes for further analysis. In general, for a region of interest, pixel intensity was averaged in two dimensions and plotted against the third to show trends in spatial variation. Frequency analysis was also performed in python using the Scipy.fft package on averaged intensities to analyze layer wise variation. The averaging of intensity across axes allows for identification of trends that might not be distinguished in a single layer.

Curvature Measurements

Curvature measurements of sintered bars were taken using the arc measurement tool on a Keyence VHX-7000 optical microscope (Figure 9). Based on the measured arc length (L) and angle(θ), curvature (κ) was calculated with Equation 1, where length is in meters, and the angle is in radians.

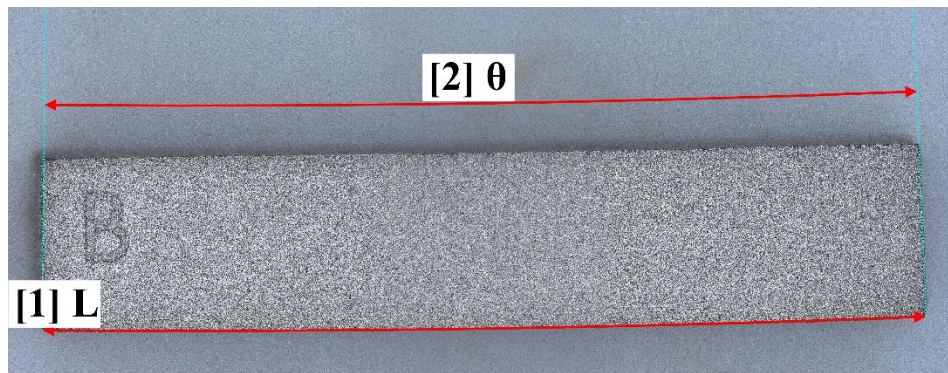


Figure 9. Example of bar, from Figure 4b, measured with the arc measurement tool. Measurement [1] is the arc length of the section, and [2] is the angle of the arc.

$$\kappa = \frac{\theta}{L} \quad \text{Equation 1}$$

Results and Discussion

Shelled Part Density Trends

Figure 10 shows overall density measurements as a function of the percentage unbound powder trapped in the part by volume for several batches of cubes. There is bed to bed variation in density, likely due to environmental conditions such as powder humidity level. While the smaller 5mm cubes (Figure 10) seem to show increased density with more trapped unbound powder like many of the other shelled part studies, the larger 10 mm cubes show the opposite trend. This may indicate boundary effects, at the transition regions between bound and unbound

powder, since the surface area to volume ratio is different for different cube sizes, even with the same fraction of unbound powder. For both 5 and 10 mm cubes the overall amount of density variation is small (1-2%). While there is a noticeable shift in the mean densities, the variation within each sample type is larger than the variation in mean between sample types. This may be due to differences in bed density in different regions of the print bed, inaccuracies in printed part geometry, and for smaller parts the resolution of the mass measurements plays a larger role. This uncertainty makes it difficult to draw conclusions from these trends alone.

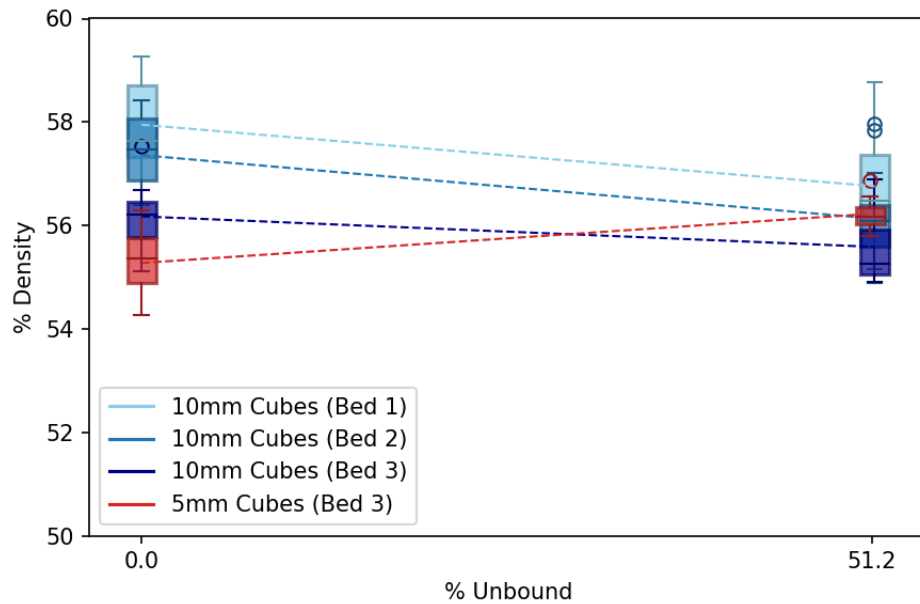


Figure 10. Estimated Green density as a function of % unbound powder for several beds of printed parts. Contrary to other studies many of the beds showed reduced overall density with the use of shelled parts. However, the smaller 5 mm parts (which were XCT scanned) show an increase in part density for shelled parts.

Shelled Micro XCT Scan Analysis

Average density measurements are easy to perform and may be useful in establishing trends for shelled parts, but they are unable to provide much information about the inner structure or internal defects of a part. In this study, micro-XCT scans were used to gain more insight into powder arrangement found in shelled BJ parts.

Figure 11 shows an X-Y slice of the micro-XCT scan for both a green and sintered 1 mm shelled cube. The layer shown is parallel to the printed layers. In both parts, the unbound area, where no binder was deposited, is distinct from the surrounding bound areas. The bound areas show more pores (dark regions) than the adjacent trapped unbound powder. The print lines are visible in both the green and sintered parts. This distinct difference indicates that the density of green bound / printed regions is lower than the spread powder density. Thus, the increased density of shelled parts after sintering might not be an effect of residual binder left behind in the

sintering process as speculated [7, 9, 10], at least for these materials. In Figure 11, both the green and sintered parts have large observable pores in the bound regions and visible lines in the printhead direction (Y) that are likely caused by binder disrupting the powder during the print process. This is consistent with high-speed X-Ray imaging results reported previously [11, 15, 16]. However, Lawrence et al. [16] showed that the volume of powder moved during printing was relatively small compared to the volume of the primitives created, which may indicate that other factors contribute to the large differences in average density between bound and unbound regions observed in the XCT scans. One possibility is that when rolling powder over a previously printed region the partially cured layers inhibit powder compaction, resulting in low density printed regions [6].

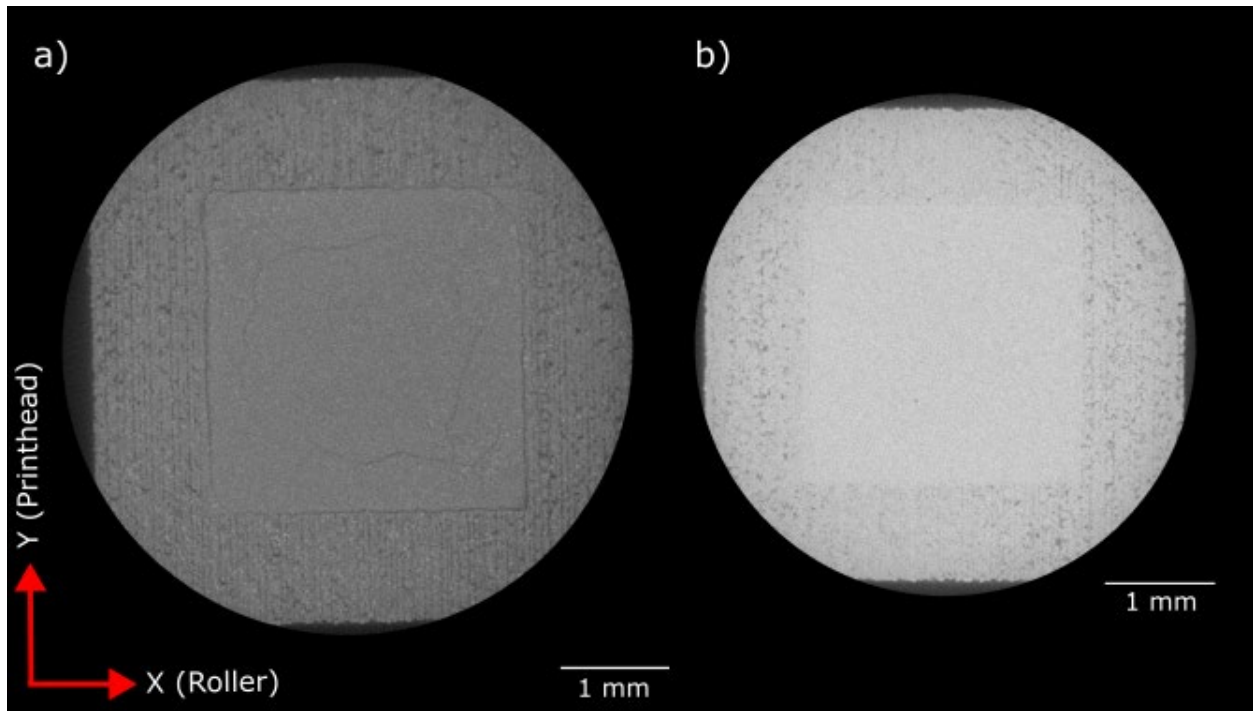


Figure 11. XY slices of Micro-XCT scans of two shelled parts printed in the same batch. a) green b) sintered to 1350C. Both show print lines and pores in the bound regions.

The XCT scans also show cracklike features in the unbound regions of the green parts. Figure 12 is an example of large cracklike features, but most of the green parts demonstrated cracking in the unbound powder to some extent. Cracklike features were especially prevalent at the top surface of an unbound cavity. This may indicate that the cracklike features may form due to settling during handling of the green part. This could be a concern for final part quality. However, the cracklike features may heal during sintering as no large cracklike features were seen in the sintered samples, but sintered XCT scans were not performed on the exact same parts as the green scans, so this study is unable to definitively show that cracklike features in the green parts were healed during sintering.

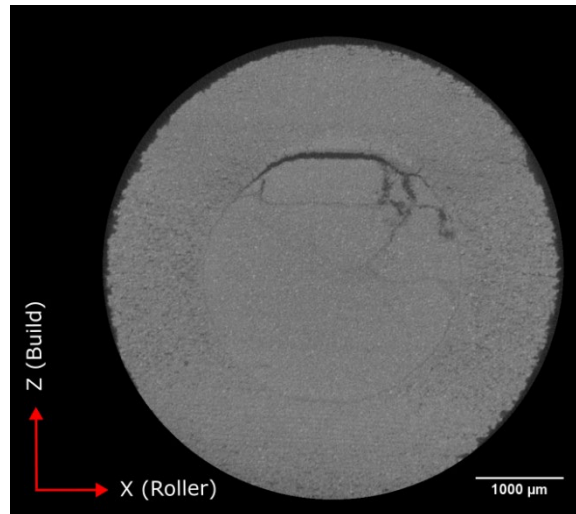


Figure 12. Severe crack-like features visible in a XZ slice XCT of green shelled part, this cracklike feature was at the top of the unbound cavity during printing, and powder has settled. Other samples had similar defects to varying extents.

Further insight into density variations can be obtained by analyzing the spatial variation in intensity of the XCT scans. The pixel intensity variation in the XCT images should correlate with density. Figure 13 shows that averaged XCT scan pixel intensity is higher in the unbound regions for green parts indicating higher density in the spread powder bed than in the printed region. Some studies make assumptions that the density of each region (bound and unbound) is homogenous [17], but as seen by the dips at the transition regions between bound and unbound powder in Figure 13, there are low density regions in the unbound powder close to the bound walls. These low-density regions are more pronounced in the roller direction but appear to be similar on both the leading and trailing edge. This could support the theory that poor rolling compaction on or near bound areas is causing reduced density [6]. As feature sizes decrease these low-density regions may become a larger volume fraction of the part and have a larger impact on final properties.

In the printing direction, there is smaller drop in intensity near the bound/unbound interface, but there is a gradient in intensity from one side to another. Density gradients perpendicular to the roller direction have not been reported previously, but density is known to be impacted by the quantity of powder deposited on the bed. The Innovent deposits powder from a hopper and the quantity of powder might not be uniform along the entire width of the hopper. However, the slope and intensity could also be a result of imaging artifacts rather than density changes. Further studies are needed to understand this issue.

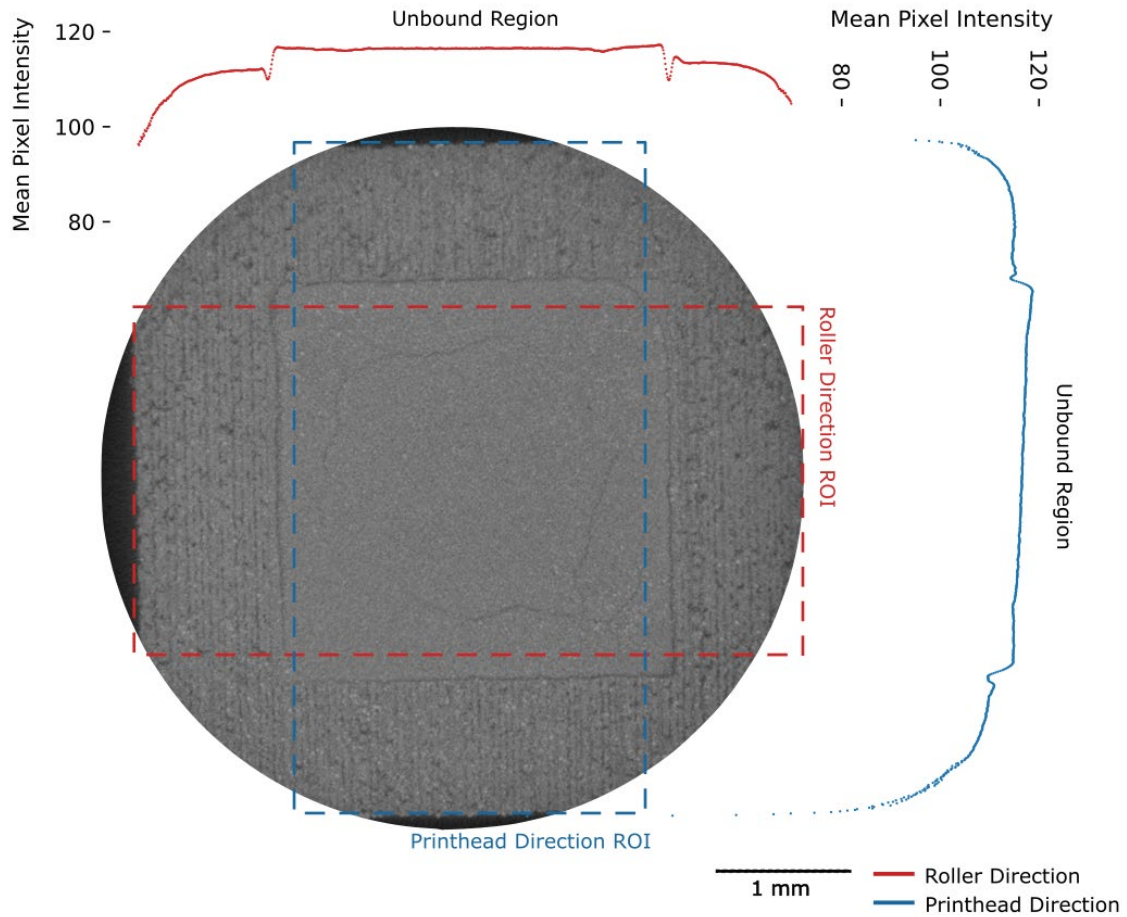


Figure 13. Plots of mean pixel intensity overlaid with a single slice of the XCT image for a) Roller direction (red) and b) Printhead direction (blue) of a green shelled part. Pixel intensity was averaged across all slices of the XCT scan in the region of interest (ROI) indicated by the dashed lines. The average intensity declines at the ends of the scans due to the circular shape of the scanned region.

In sintered shelled parts of the same type, the crack-like defects observed in green parts were not observed which may mean that they disappear during sintering. Figure 14 shows the same type of mean pixel intensity profiles as Figure 13 for a sintered part. The large dips in intensity near the boundary are gone, but there is still an observable difference between the bound and unbound regions and a small transition region near the boundary. In the sintered part, the profile appears to be the same in both printhead and roller directions.

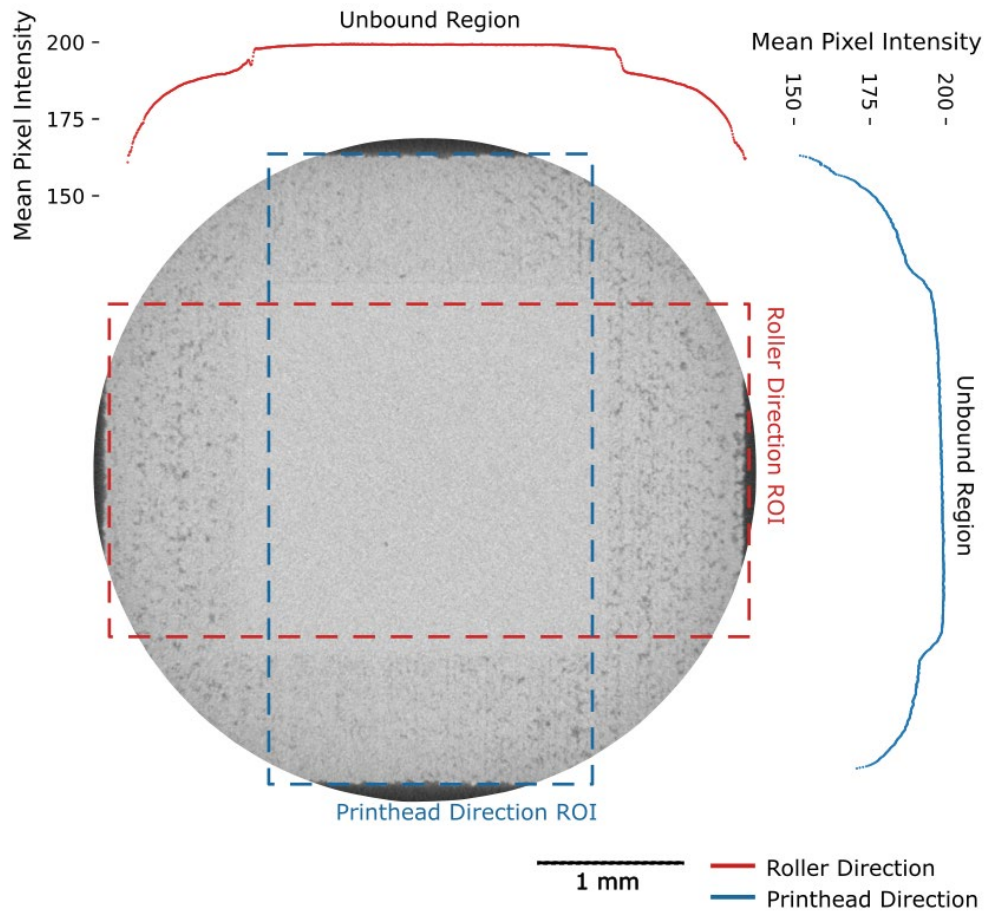


Figure 14. Plots of mean pixel intensity in a) Roller direction (red) b) Printhead direction (blue) of a sintered shelled part. Pixel intensity was averaged across all slices of the XCT scan in the region of interest (ROI) indicated by the dashed lines.

Similarly, Figure 15 shows both the green and sintered parts also have a dip in pixel intensity corresponding to the bound region when looking at the Z-direction. In the green part (Figure 15a), there is an especially large dip in pixel intensity immediately below the horizontal bound wall, which supports the idea of cracklike features or settling in the unbound regions. Visually, layer lines can be observed in the bound regions of the green shelled parts. However, using a FFT analysis (Figure 15a) it is observed that periodic pixel intensity variation at the expected period based on the print layer size (40 μ m) is evident in the both the bound and unbound regions, but the amplitude of variation is approximately 5 times larger in the bound regions. Other studies have shown that powder size and layer thickness may influence the detectability of layer wise density variation [17]. In the sintered part (Figure 15b), layer lines are still detectable in the bound region but have shrunk proportionally to the overall part shrinkage. In the unbound regions of the sintered parts, the dominate frequency of the FFT analysis is far too large (\sim 266 μ m) to be caused by single layer variation, which indicates the layer lines defects have largely disappeared.

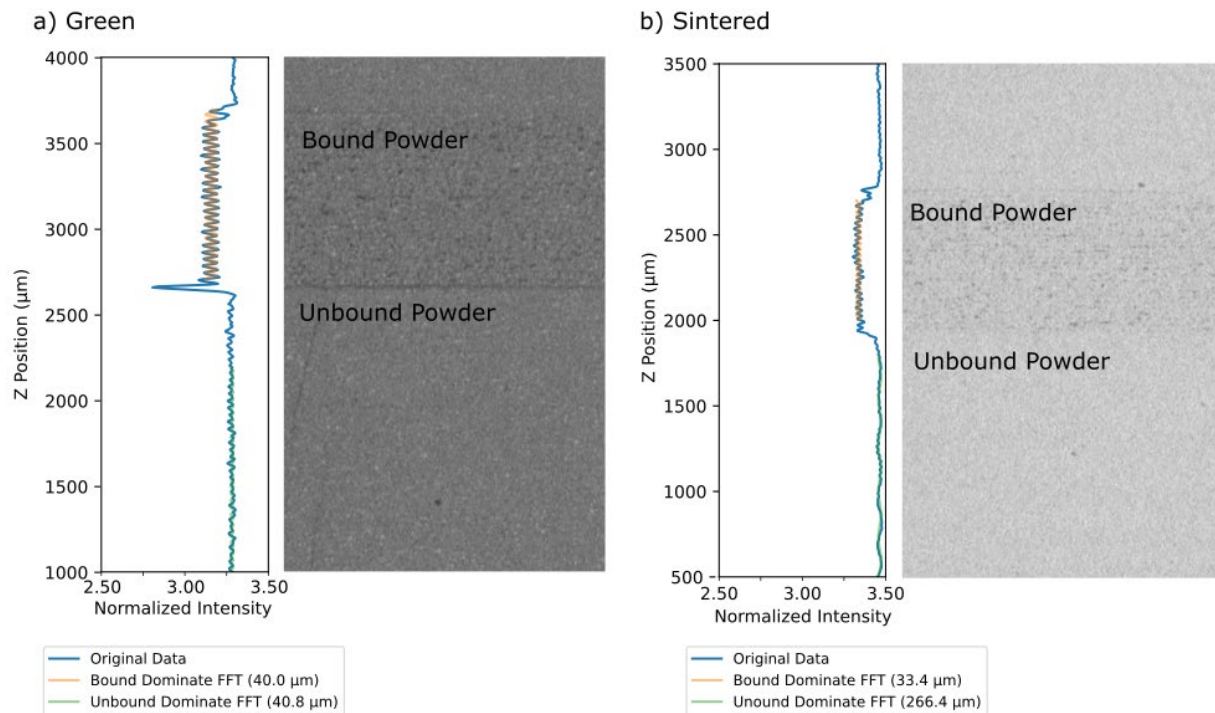


Figure 15. Z-direction variation in pixel intensity, with FFT analysis for each region, overlaid on a slice of the XCT imagery. a) Green shelled part. b) Sintered shelled part.

Figure 16 compares the normalized pixel intensity in each direction for the slot parts printed with the long direction of the slot parallel and perpendicular to the roller. The X-Ray intensity profile shows similar differences between bound and unbound regions (Figure 16a, b) for both print orientations. The low-density region immediately adjacent to the bound/unbound boundary only appears when the long axis of the slots is parallel to the rolling direction (Figure 16b), and does not have the low intensity spikes near the boundaries between bound and unbound powder observed in the original green shelled part with larger unbound regions. However, the larger 1.5mm roller direction slots do display these dips (Figure 16b), like the green shelled part when rolling along the long-direction of the feature. This further shows that rolling compaction is playing a role in part densification, especially for larger unbound regions. The small 0.75 mm slots may display different behavior because they are small relative to the roller diameter (12 mm). These results show that rolling can impact powder bed density near boundaries and that the effects are size dependent.

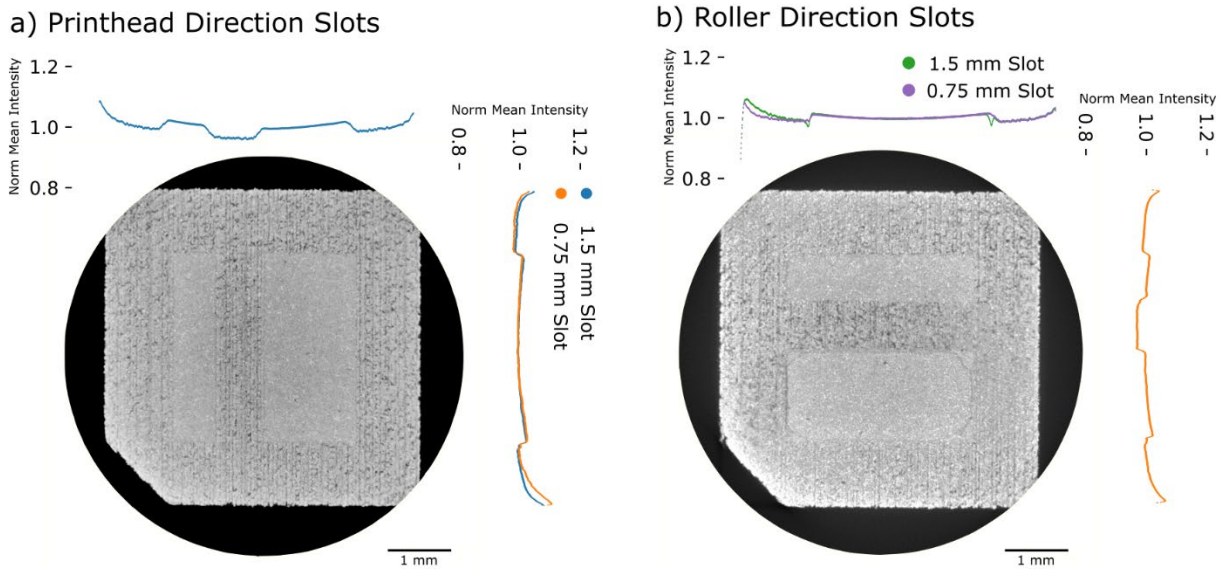


Figure 16. Average X-ray intensity profiles for shelled slot parts. Higher intensity corresponds to higher density. a) The short axis of the slots with unbound powder is aligned to the roller direction. b) The long axis of the unbound powder slots is aligned to the roller direction.

Shell Induced Curvature

Another consideration with using shelled geometry to improve print quality, is evaluating if differences in sintering rates between bound and unbound regions cause shape changes during sintering. To test this idea two types of asymmetrical bars were printed. Their dimensions are identical, but one type has the unbound region towards the front during printing and sintering, and the other type is reversed with the unbound region towards the back of the part (CAD models in Figure 17). This controls for differences in printer or furnace behavior based on orientation. For both types of parts, the sintered density was ~96.1% of bulk SS316.

As seen in Figure 17, these asymmetrical parts consistently showed a slight curvature towards the unbound region, regardless of the side of the part. The effect measured on these parts isn't large, but as part aspect ratio increases, it may be a bigger problem. One explanation for this behavior is that the unbound regions sinter and shrink faster than the nearby bound regions and cause the bound regions to warp around them. More exploration is needed, but this could be due to difference in density or because of the reduced carbon content in the unbound regions. Previous studies have shown that the presence of carbon reduces shrinkages [18, 19].

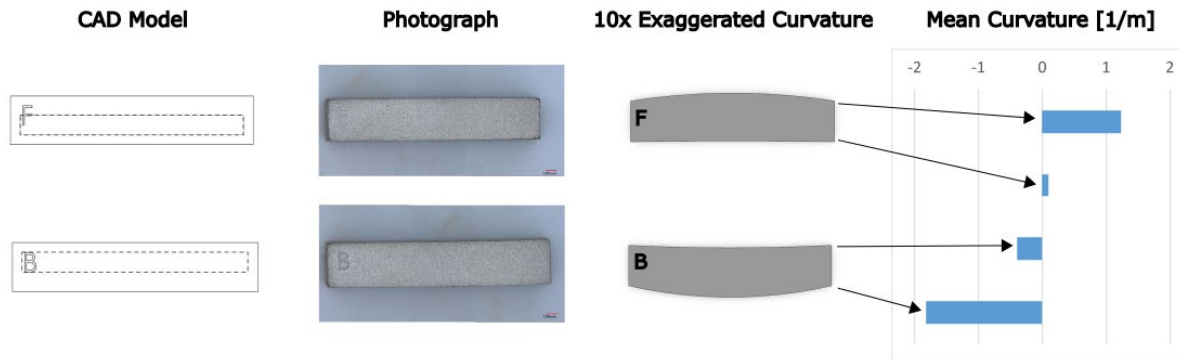


Figure 17. Original CAD model (dashed lines indicate unbound region), photographs of sintered parts, exaggerated curved CAD models, and mean curvature of each edge of the sintered parts for the two types of asymmetrical bars (F- Unbound region in the front during both printing and sintering, B- Unbound region in back). It is observed that there is increased curvature on the side with a thicker bound wall towards the unbound cavity.

Conclusions

This work shows that printing impacts the density of the green parts. Micro-XCT images show that the density of bound regions is consistently lower than unbound powder that is trapped inside the part. The density varies with height in the layer direction with a periodicity that matches the layer thickness. Additionally, the density at the boundary between bound and unbound regions was lower than seen in the interior of either printed or unbound powder regions. Cracklike features were also visible in unbound regions. Sintering reduces these variations, but density differences between bound and unbound regions persist as has been reported previously. Additionally, asymmetry in the bound/unbound regions was shown to cause curvature in the sintered parts.

Even though boundary effects are reduced in sintered parts, they could limit the usefulness of shelled printing if the size or orientation of the unbound regions reduces the benefits. This has repercussions on the shape and size of unbound regions that are advantageous in shelled printing. Most studies print shelled cubes or cylinders but propose that shell printing could be used for all/any geometries. This may not be true. Additionally, small features may be hard to achieve with shell printing because there is a minimum practical wall thickness. The benefits in small regions may also be reduced relative to studies in large parts.

Acknowledgments

This work made use of Nanofab EMSAL shared facilities of the Micron Technology Foundation Inc. Microscopy Suite sponsored by the John and Marcia Price College of Engineering, Health Sciences Center, Office of the Vice President for Research. The research was supported by the National Science Foundation under grant CMMI-1946724.

References

- [1] M. Ziaee, N.B. Crane, Binder jetting: A review of process, materials, and methods, *Additive Manufacturing*, 28 (2019) 781-801.
- [2] I. Gibson, Rosen, David, Stucker, Brent, *Additive Manufacturing Technologies*, (2015).
- [3] J. Lawrence, C. Inkley, K. Fezzaa, S.J. Clark, N.B. Crane, Observations of Binder Jetting Defect Formation Using High-Speed Synchrotron X-Ray Imaging, 2022 International Solid Freeform Fabrication Symposium, (2022).
- [4] S. Mirzababaei, S. Pasebani, A review on binder jet additive manufacturing of 316L stainless steel, *Journal of Manufacturing and Materials Processing*, 3 (2019) 82.
- [5] M. Ziaee, E.M. Tridas, N.B. Crane, Binder-Jet Printing of Fine Stainless Steel Powder with Varied Final Density, *JOM*, 69 (2017) 592-596.
- [6] M. Li, G. Miao, W. Du, Z. Pei, C. Ma, Difference between powder bed density and green density for a free-flowing powder in binder jetting additive manufacturing, *Journal of Manufacturing Processes*, 84 (2022) 448-456.
- [7] K.M. Rahman, A. Wei, H. Miyanaji, C.B. Williams, Impact of binder on part densification: Enhancing binder jetting part properties through the fabrication of shelled geometries, *Additive Manufacturing*, 62 (2023) 103377.
- [8] N.J. Salim, I. Arretche, K.H. Matlack, A process to spatially control the fraction of SS420 and bronze phases in binder jet infiltrated parts, *Journal of Manufacturing Processes*, 85 (2023) 612-622.
- [9] I. Rishmawi, M. Salarian, M. Vlasea, Tailoring green and sintered density of pure iron parts using binder jetting additive manufacturing, *Additive Manufacturing*, 24 (2018) 508-520.
- [10] Y. Mao, C. Cai, J. Zhang, Y. Heng, K. Feng, D. Cai, Q. Wei, Effect of sintering temperature on binder jetting additively manufactured stainless steel 316L: densification, microstructure evolution and mechanical properties, *Journal of Materials Research and Technology*, 22 (2023) 2720-2735.
- [11] N.D. Parab, J.E. Barnes, C. Zhao, R.W. Cunningham, K. Fezzaa, A.D. Rollett, T. Sun, Real time observation of binder jetting printing process using high-speed X-ray imaging, *Scientific reports*, 9 (2019) 2499.
- [12] H.N. Emady, D. Kayrak-Talay, J.D. Litster, A regime map for granule formation by drop impact on powder beds, *AIChE Journal*, 59 (2013) 96-107.
- [13] T. Do, T.J. Bauder, H. Suen, K. Rego, J. Yeom, P. Kwon, Additively manufactured full-density stainless steel 316L with binder jet printing, in: *ASME 2018 13th International*

Manufacturing Science and Engineering Conference, MSEC 2018, June 18, 2018 - June 22, 2018, American Society of Mechanical Engineers (ASME), College Station, TX, United states, 2018, pp. Manufacturing Engineering Division.

[14] A.D. Zwiren, T.F. Murphy, Comparison of SS-316L PM material processed via binder jetting with SS-316L powder processed by pressing and sintering, *International Journal of Powder Metallurgy*, 54 (2018) 39-50.

[15] C.G. Inkley, J.E. Lawrence, N.B. Crane, Impact of controlled prewetting on part formation in binder jet additive manufacturing, *Additive Manufacturing*, 72 (2023) 103619.

[16] J.E. Lawrence, M.P. Lawrence, N. Crane, Experimental Study of the Impact of Droplet and Printing Parameters on Line formation in Binder Jetting, (2024).

[17] G. Miao, M. Moghadasi, M. Li, Z. Pei, C. Ma, Binder jetting additive manufacturing: powder packing in shell printing, *Journal of Manufacturing and Materials Processing*, 7 (2022) 4.

[18] N.B. Crane, Strengthening porous metal skeletons by metal deposition from a nanoparticle dispersion, in, *Massachusetts Institute of Technology*, 2005.

[19] N.B. Crane, J. Wilkes, E. Sachs, S.M. Allen, Improving accuracy of powder-based SFF processes by metal deposition from a nanoparticle dispersion, *Rapid Prototyping Journal*, 12 (2006) 266-274.